Journal of Colloid and Interface Science 630 (2023) 629–637

Contents lists available at ScienceDirect

Journal of Colloid and Interface Science

journal homepage: www.elsevier.com/locate/jcis

Facile polymerization in a bicellar template to produce polymer nano-rings

Chung-Hao Liu [a,1], Catherine Cheu [a,1], John G. Barker [b], Lin Yang [c], Mu-Ping Nieh [a,d,*]

[a] Polymer Program, Institute of Materials Science, University of Connecticut, Storrs, CT 06269, United States
[b] Center for Neutron Research, National Institute of Standard and Technology, Gaithersburg, MD 20899, United States
[c] National Synchrotron Light Source – II, Brookhaven National Laboratory, Upton, NY 11973, United States
[d] Department of Chemical and Biomolecular Engineering, University of Connecticut, Storrs, CT 06269, United States

GRAPHICAL ABSTRACT

Crosslinked polymer nano-rings are produced in well-defined discoidal bicelles. The enhanced immiscibility in the planar region drives the hydrophobic polymers to the fluidic rim. The platform can be generalized for synthesis of other hydrophobic polymer nano-rings.

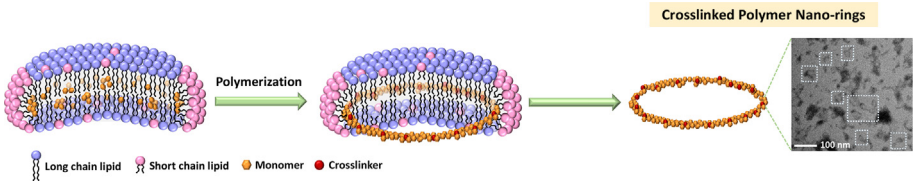

ARTICLE INFO

Article history:
Received 23 July 2022
Revised 24 September 2022
Accepted 26 September 2022
Available online 10 October 2022

Keywords:
Discoidal bicelles
Emulsion polymerization
Radical polymerization
SAXS/SANS
Contrast variation

ABSTRACT

Hypothesis: A well-defined discoidal bicelle composed of three lipids, specifically zwitterionic long-chain 1,2 dipalmitoyl phosphocholine (DPPC) and short-chain 1,2 dihexanoyl phosphocholine (DHPC) doped with anionic 1,2 dipalmitoyl phosphoglycerol (DPPG) provides a generalized template for the synthesis of hydrophobic polymer nano-rings. The lipid molar ratio of DPPC/DHPC/DPPG is 0.71/0.25/0.04. The detailed investigation and discussion were based on styrene but tested on three other vinyl monomers.
Experiments: The structure of nano-rings is identified through the detailed analysis of small angle X-ray/neutron scattering (SAXS and SANS) data and transmission electron micrographs (TEM), supported by the differential scanning calorimetric (DSC) data before and after polymerization. The investigation covers samples with a styrene-to-lipid ratio ranged varied from 1:50 to 1:10.
Findings: The styrene monomers are initially located at both the discoidal planar (long-chain lipid rich) and rim (short-chain lipid rich) regions. During polymerization, they migrate to the more fluid rim regionsection. The formation mechanism involves the interplay of hydrophobic interaction, mismatched miscibility of polystyrene between the ordered and disordered phases, and crystallinity of the long lipid acyl chains. This facile synthesis is proven applicable for several hydrophobic monomers. The well-defined nano-rings greatly enhance the interfacial area and have the potential to be the building blocks for functional materials, if monomers are incorporated with desirable functions, for future applications.

* Corresponding author at: Polymer Program, Institute of Materials Science, and Department of Chemical and Biomolecular Engineering, University of Connecticut, Storrs, CT 06269, United States.
E-mail addresses: chung.liu@uconn.edu (C.-H. Liu), catherine.cheu@uconn.edu (C. Cheu), john.barker@nist.gov (J.G. Barker), lyang@bnl.gov (L. Yang), mu-ping.nieh@uconn.edu (M.-P. Nieh).
[1] Chung-Hao Liu formulated the concept, collected all the scattering data and DSC data, performed the data analysis and composed the first edition of this article. Catherine Cheu developed the scattering models of 5LCSD, SR-CSD and helped with SANS data analysis. They contributed this project equally. John G. Barker and Lin Yang set up the SANS and SAXS configurations for this project, respectively. Mu-Ping Nieh oversees the whole project.

https://doi.org/10.1016/j.jcis.2022.09.141
0021-9797/

1. Introduction

Emulsion polymerization is a highly efficient and environmentally-friendly process, which is applicable to hydrophobic monomers, including styrene, vinyl acetate, acrylate *etc*. [1,2], to yield high molecular weights at a rapid reaction rate due to the fact that the free radicals grow in a relatively isolated environment [3]. Emulsions are normally utilized as the templates for spherical latexes [4–6], polymeric capsules [2,7–10], or porous materials [11–13] with length scales above 50 nm to several microns. The great challenge of emulsion polymerization is thermodynamic instability of monomer droplets, causing coalescence of droplets (known as Ostwald ripening) driven by minimization of the interfacial area [14–16]. Although the Pickering emulsifiers [17] can protect the emulsions against coalescence, controllable sizes of droplets < 50 nm remained difficult [18,19].

Polymerization-induced self-assembly (PISA)[20] presents another approach to generate polymeric nanoparticles with tunable sizes and shapes [21–23]. Morphological transitions from spheres to various high order structures, such as worm-like micelles, lamellae, vesicles, toroids and other more complex morphologies have been reported [24–28]. However, the challenge of PISA lies in controlling and predicting the morphology, which requires a comprehensive study of the phase diagram [29].

Lipids can robustly self-assemble into well-defined morphologies, thus serving as a good template for controllable polymerization [30]. It has been reported that a lipid mixture, bicelle, composed of long-chain (**L**) and short-chain (**S**) lipids with a molar ratio in the range of $2 \leq [L]/[S] \leq 5$, can yield uniform discs (low polydispersity in diameter) with high stability [31,32]. The formation mechanism of nanodiscs is attributed to the hydrophobic interactions, segregation of **S** from **L** lipids, appropriate molecular spontaneous curvatures (low-curvature **L** and high-curvature **S**) and sufficient surface charged density [33]. Tekobo et al. reported the synthesis of crosslinked polystyrene (**PS**) discs in the bicelle made of dimyristoyl phosphatidylcholine (DMPC, di-C_{14}PC) and dihexanoyl phosphocholine (DHPC, di-C_6PC)[34,35]. The conclusion was drawn based on a few disk-like particles in the transmission electron micrographs (TEM). It is not clear if **PS** disks represent the majority of morphological distribution. Contrarily, it has been reported that hydrophobic nanoparticles such as Au-clusters [36,37], metallo-supramolecules [38], or quantum dots (QDs) [39] are preferably located at the high-curvature fluid rim of bicelles made of 1,2-dipalmitoyl-*sn-glycero*-3-phosphocholine (DPPC, di-C_{16}PC) and DHPC doped with long-chain anionic 1,2-dipalmitoyl-*sn-glycero*-3-phospho-(1′-*rac*-glycerol) (DPPG, di-C_{16}PG). The different outcomes of the preferred locations for foreign species in bicelles lead to an important question: how do discoidal bicelles entrap other hydrophobic molecules or nanoparticles?

Here, we report a detailed study to understand the internal distribution of hydrophobic monomers (prior to polymerization) and polymers (after polymerization) in a DPPC/DPPG/DHPC bicellar system. Note that the melting transition temperature, T_m, of DPPC (41 °C) is higher than that of DMPC (23 °C). The bicellar nanodisc is expected to be more stable, allowing the polymerization to take place below the T_m. Well-defined **PS** nano-rings were found in the bicelles as characterized by small angle X-ray scattering (SAXS), small angle neutron scattering (SANS) and transmission electron microscopy (TEM). The structure agrees with the unique variation between the high-sensitive differential scanning calorimetric (DSC) data before and after polymerization. This approach is applicable to other hydrophobic monomers and can be a generalized facile method for manufacturing functional polymer nanorings in the future.

2. Materials and Methods

2.1. Materials

1,2-dipalmitoyl-*sn-glycero*-3-phosphocholine (DPPC), 1,2-dihexanoyl-*sn-glycero*-3-phosphocholine (DHPC) and 1,2-dipalmitoyl-*sn-glycero*-3-phospho-(1′-*rac*-glycerol) (sodium salt) (DPPG) were purchased from Avanti Polar Lipids (Alabaster, AL) and used without further purification. The chemical structures of DPPC, DHPC, and DPPG are presented in Fig. 1. It is known that anionic DPPG stabilizes the discoidal morphology of bicelles [33]. The styrene, divinylbenzene (DVB, crosslinker), lithium phenyl (2,4,6-trimethylbenzoyl) phosphinate (initiator), 4-methylstyrene, vinyl acetate, and dodecyl methacrylate were purchased from Sigma-Aldrich. The DVB crosslinker was used for all types of vinyl monomers in this study. The deuterium oxide (D_2O) and deuterated styrene (styrene-d_8) were purchased from Cambridge Isotope Laboratories. Acidic and basic aluminum oxide were utilized to remove the inhibitor from monomers. These two materials were also purchased from Sigma-Aldrich.

2.2. Structure of monomers encapsulated bicelles before and after polymerization

The bicellar mixture contains three types of lipids: DPPC, DPPG and DHPC with a molar ratio of total long-chain to short-chain lipid, Q (≡[DPPC]+[DPPG])/[DHPC]) of 3 and a molar ratio of long-chain anionic lipid to total long-chain lipid, R (≡[DPPG]/([DPPC]+[DPPG])) of 0.05. All dry lipid powders were homogeneously dissolved in chloroform with appropriate ratio and amount. After the removal of most chloroform by using nitrogen, individual samples were subjected to vacuum overnight [31]. Afterwards, the vinyl monomer (styrene, vinyl acetate, dodecyl methacrylate, or methyl styrene) and DVB (at a molar ratio of 7:1) was added to the dried lipids at three molar ratios ≡([monomer]+[DVB])/[total lipid], i.e., 1:50, 1:20 and 1:10, respectively. The individual samples were then hydrated to a lipid concentration, C_{lp} of 20.0 wt% by H_2O (for SAXS, TEM, WAXS and DSC studies), or D_2O or contrast-matched water (for SANS study) for stock solutions. Two groups of samples were polymerized at different C_{lp} (either 20.0 or 1 wt %). The outcomes were not significantly different except for **SB-10**. The samples with ([monomer]+[DVB])/[total lipid] = 1/50, 1/20 and 1/10 are denoted by **SB-50**, **SB-20**, and **SB-10**, respectively. Other monomer-containing (vinyl acetate, dodecyl methacrylate, and methyl styrene) bicellar mixtures were prepared with ([monomer]+[. The high-C_{lp} samples (i.e., 20 wt%) underwent 10 thermal cycles between 4 and 60 °C with vortexing at each cycle until they were fully dissolved in water, where the solution is fluid at low T (≤room T) but viscous at high T (≥35 °C). The rheological response has been reported in literature [31] and is attributed to the structural transformation of bicelles into interpenetrated perforated lamellae [40,41] upon increasing T. It should be noted that the structures are reversible upon T-cycling at this high C_{lp} (=20 wt %). [31,42] Polymerization was initiated by a photochemical initiator, lithium phenyl-2,4,6-trimethylbenzoylphosphinate, with a monomer-to-initiator ratio of 1:2 due to the existing oxygen effect

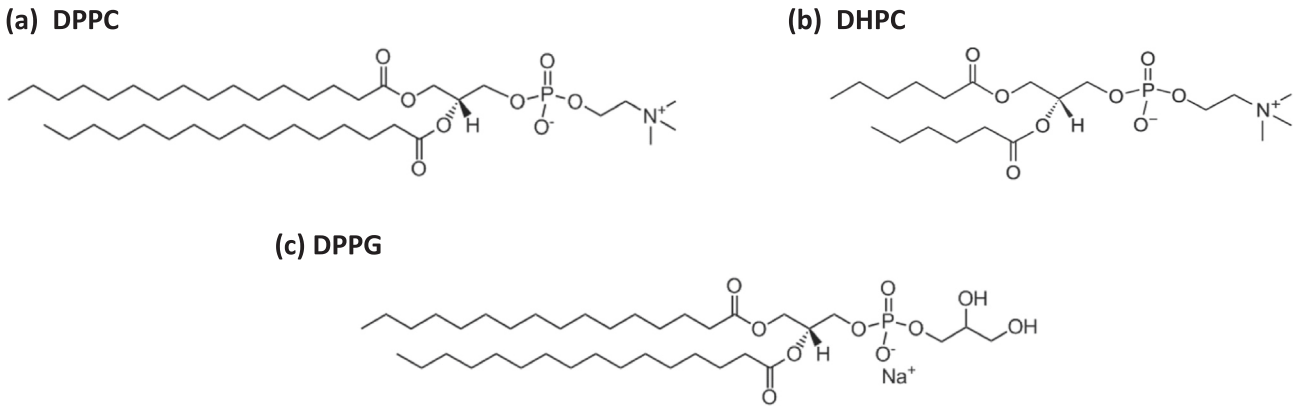

Fig. 1. Chemical structures of (a) DPPC, (b) DHPC, and (c) DPPG.

[43] in a water bath at 25 °C for 48 h. The wavelength of the UV lamp is 365 nm.

The lipid template can be removed by the following procedure: 40 μL of 1 % **PS/**bicelle (hereinafter referred to as **PSB**) aqueous solution was dried with purged nitrogen and further dried at 60 °C under vacuum overnight. The samples were then washed with methanol to precipitate nano-rings for three times.

2.3. Polymerization monitored by UV–vis

The extent of polymerization was evaluated by the UV–vis absorbance at 282 nm, reflecting the quantity of styrene. [35,44] The total volume for evaluating polymerization is ~ 1 mL. Multiple 5 μL aliquots were taken from the same mixture (styrene/bicelle) at 0, 1, 5, 7, 24, and 48 h and were extracted by 1 mL of chloroform. The UV–vis absorption spectra were measured using PerkinElmer Lambda 1050 from 200 to 500 nm. Complete polymerization was determined by the invariant absorbance at 282 nm.

2.4. Transmission electron microscopy (TEM)

The TEM images were acquired using FEI Tecnai T12 with accelerating voltage 80 kV. Polymerization at C_{lp} = 1 wt% of **PSB-50**, **PSB-20**, Poly(vinyl acetate) (PVAc)-bicelle, Poly(dodecyl methacrylate) (PC12MA)-bicelle, and Poly(4 methyl styrene) (P4MS)-bicelle solutions were first diluted to C_{lp} = 0.002 wt%. Then, 3 μL of the diluted solution was deposited on the 200 mesh copper grids covered with carbon film. The samples were negatively stained by 0.5 wt% of uranyl acetate before imaging. Noted that the lipid-removed **PSB-50**, **PSB-20** samples were not negatively stained. The grids were dried at room temperature overnight.

2.5. Small angle X-ray scattering (SAXS)

SAXS experiments were conducted at the 16ID-LiX Beamline (National Synchrotron Light Source II, located at the Brookhaven National Laboratory, Upton, NY). The C_{lp} of all samples is 1 wt%. The SAXS measurements were conducted using the standard flow-cell for solution scattering setup with the energy of synchrotron to be 13.5 keV. SAXS intensity is expressed as a function of scattering vector, q defined as , where θ is the scattering angle and λ is the wavelength, covering a q range from 0.005 to 2.5 $Å^{-1}$. Data reduction was obtained through radial average of intensity with respect to the beam center using Jupyter Notebook [45]. The background subtraction and transmission correction were performed by minimizing the intensity of the water peak at ~ 2.0 $Å^{-1}$.

2.6. Contrast-matched (CM) SANS

The contrast-matched (CM) SANS experiment provides detailed internal structural information of the bicelle as the neutron scattering length density (NSLD) of solvent, $\rho_{solvent}$, approximates the average NSLD of lipid (DPPG, DPPC and DHPC) mixture, which is 2.72 $\times 10^{-7}$ $Å^{-2}$, calculated by an online SLD calculator (https://www.ncnr.nist.gov/resources/activation/). [42] The CM composition of D_2O/H_2O for the bicelle is therefore determined to be 12/88 by volume. It should be noted that contrast-matched condition greatly reduces the scattered intensity, yielding very noisy low-q data. However, such approach highlights the location of styrene or **PS** in bicelles if deuterated styrene is used as the only scattering contribution is presumably from **PS**. It should be noted that structure factor can be considered to be unity at the CM condition, i.e., interparticle interaction is negligible even at high C_{lp} [46].

To increase the scattering intensity, CM samples were examined at a high C_{lp} (=20 wt%). The SANS measurements were performed at CHRNS VSANS [located at the National Institute of Science and Technology (NIST) center for neutron research (NCNR, Gaithersburg, MD)] with the average neutron wavelength of 5 Å and a wavelength spread of 12.5 %, yielding a q range from 0.024 to 0.8 $Å^{-1}$. The front and middle detectors were used for low and high q data collection, respectively. The 2D raw data were corrected by the detector sensitivity, background, scattering and transmission of empty cells and sample transmission. The corrected data were then circularly averaged to produce 1D profiles and the intensity was put on the absolutely scale based on the incident beam flux. The data reduction package was provided by NCNR using the IGOR macros with IGOR Pro software.

2.7. Differential scanning calorimetry (DSC)

DSC measurements were conducted using a NanoDSC (TA Instruments, New Castle, DE). All the samples were measured at C_{lp} = 1.0 wt%. The 0.5 mL of DI water and sample were loaded in the reference and sample cells, respectively. The experimental pressure was kept at 3 atm. Before each measurement, samples were equilibrated at 30 °C for 10 min. The data of both sample and solvent background were collected from 30 to 55 °C at the rate of 1 °C/minute in sequence to ensure the consistency of instrument performance. The baseline was adjusted by using TA Instrument software.

2.8. Wide-angle X-ray scattering (WAXS)

Oxford Diffraction Xcalibur PX Ultra (transmission mode) were used for WAXS measurements with Onyx detector (CuKα radiation

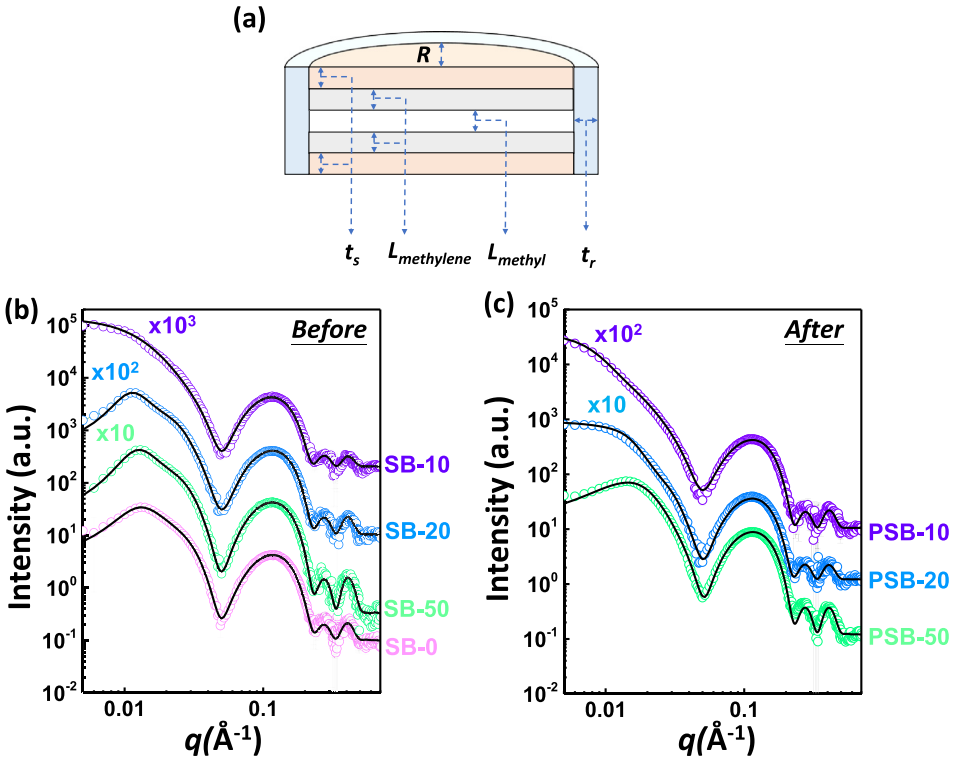

Fig. 2. (a) The schematic of Five-Layer Core Shell Discoidal (5LCSD) model. The SAXS patterns of **SB-0**, **SB-50**, **SB-20**, and **SB-10** (b) before and (c) after polymerization (**PSB-50**, **PSB-20**, and **PSB-10**). Noted that the polymerization performed at lipid concentration of 1 wt%.

1.54 Å, double mirror focusing, 35 kV and 35 mV). The **SB-** and **PSB-** samples (C_{lp} = 20 wt%) were loaded in 1-mm quartz capillaries, and sealed by wax. The scattering patterns were analyzed by PDXL software [47]. It should be mentioned that the WAXS data of water background were subtracted from those of the individual samples.

3. Results and discussion

3.1. SAXS measurements – the global structure

The morphologies of pristine bicelles (**SB-0**), the styrene-to-lipid ratios of 1:50 (**SB-50**), 1:20 (**SB-20**), and 1:10 (**SB-10**) with 1 wt% lipid concentration (C_{lp}) were first evaluated by SAXS (Fig. 2). The SAXS data exhibit a similar pattern for q > 0.04 Å^{-1}, corresponding to the invariant lipid bilayer structure, but the low-q data (q < 0.03 Å^{-1}) exhibits some deviation, suggesting different discoidal radii. All SAXS data were fitted by five-layer core shell discoidal model [5LCSD, Fig. 2(a)]. [48] The five layers account for two phosphate shells, two layers of ordered, high-density hydrocarbons and one centered layer of less-ordered, low-density hydrophobic regions. Note that only this model can simultaneously describe both low- and high- q SAXS data and reveal detailed internal bilayer structure and electron density of each region of the disc. [48] The low-q peak at ~ 0.01 Å^{-1} originates from structure factor, $S(q)$ due to the strong Coulombic interaction among bicelles. The Hayter-Penfold mean spherical approximation (H-PMSA) model is employed to estimate $S(q)$ [49,50] due to the Coulombic interaction of DPPG. It should be noted that structure factor mainly affects the scattering pattern at q < 0.02 Å^{-1} and has weak influence on characteristic length < 300 Å. The best-fitting parameters (Table 1) show that the core radius (R) increases from 75 (±4) Å of **SB-0** to 110 (±3) Å of **SB-10**, consistent with the peak shift of structure factor from a higher to lower q value (i.e., increased interparticle spacing). The best fits reveal that the discoidal structure retains after the encapsulation of styrene. Polymerization of styrene was then conducted via UV (λ = 365 nm) at 25 °C for 48 h until the UV–vis absorption spectra are nearly invariant (Fig. S2), ensuring **PS** in the bicelles [35,51]. Although the SAXS patterns of the **PS**/bicelle samples (hereinafter referred to as **PSB-50**, **PSB-20** and **PSB-10**) [Fig. 2(b)] appear differently from those of their styrene counterparts, the 5LCSD model fits well to all data and the best fitting outcomes indicate that both R and rim thickness (t_r) increase compared with **SB** series (Table 1). The enlarged t_r of **PSB** samples compared to the corresponding **SB** samples suggests **PS** preferably locates at the rim of discs. The increased R in the **PSB** samples partially inherits from the **SB** samples, which are slightly larger than that of the pristine bicelle, and may also originate from the fusion between disks. It has been reported that such fusion takes place at higher T or lower lipid concentration. [32] Since polymerization is an exothermic process leading to higher temperature in the local environment of the bicelles, it promotes the fusion of the disks resulting in enhanced R in the **PSB-50**, **PSB-20** and **PSB-10** samples. The discoidal dimensions revealed in transmission electron microscopic (TEM) micrographs (Fig. S3) are consistent with SAXS best fitting results.

3.2. SANS and TEM outcomes – nano-rings structure

The CM SANS experiments were conducted to examine the location of styrene and **PS** in bicelles. Here, deuterated styrene (styrene-d_8) and protiated lipids were used to enhance the contrast. The NSLD of solvent, $\rho_{solvent}$ is adjusted to match the average NSLD of lipids, ρ_{lipid}, i.e., $\rho_{solvent} = \rho_{lipids} = 2.72\times10^{-7}$ Å^{-2} with a volume composition of H_2O/D_2O = 88/12 (Fig. S4) [42,52]. Ideally, the scattering is mainly contributed from the contrast between the **PS-***d* (or styrene-d_8) and the environment (i.e., lipids and water).

Table 1
The best fitting parameters of SAXS through 5LSCD model before and after polymerization.

Before Polymerization				
Sample	**SB-0**	**SB-50**	**SB-20**	**SB-10**
R (Å)	75 ± 4	80 ± 2	85 ± 3	110 ± 3
t_r (Å)	38 ± 3	40 ± 3	39 ± 4	46 ± 5
$L_{methylene}$ (Å)	13 ± 1	13 ± 1	13 ± 1	13 ± 1
L_{methyl} (Å)	9.1 ± 1	8.0 ± 1	8.4 ± 1	8.0 ± 1
Reduced χ^2	0.7	3.3	0.5	4.7
After Polymerization				
Sample	**PSB-50**	**PSB-20**	**PSB-10**	
R (Å)	95 ± 6	169 ± 4	210 ± 5	
t_r (Å)	54 ± 2	56 ± 3	65 ± 3	
$L_{methylene}$ (Å)	13 ± 1	13 ± 1	13 ± 1	
L_{methyl} (Å)	8.2 ± 1	8.0 ± 1	8.0 ± 1	
Reduced χ^2	2.3	3.1	1.7	

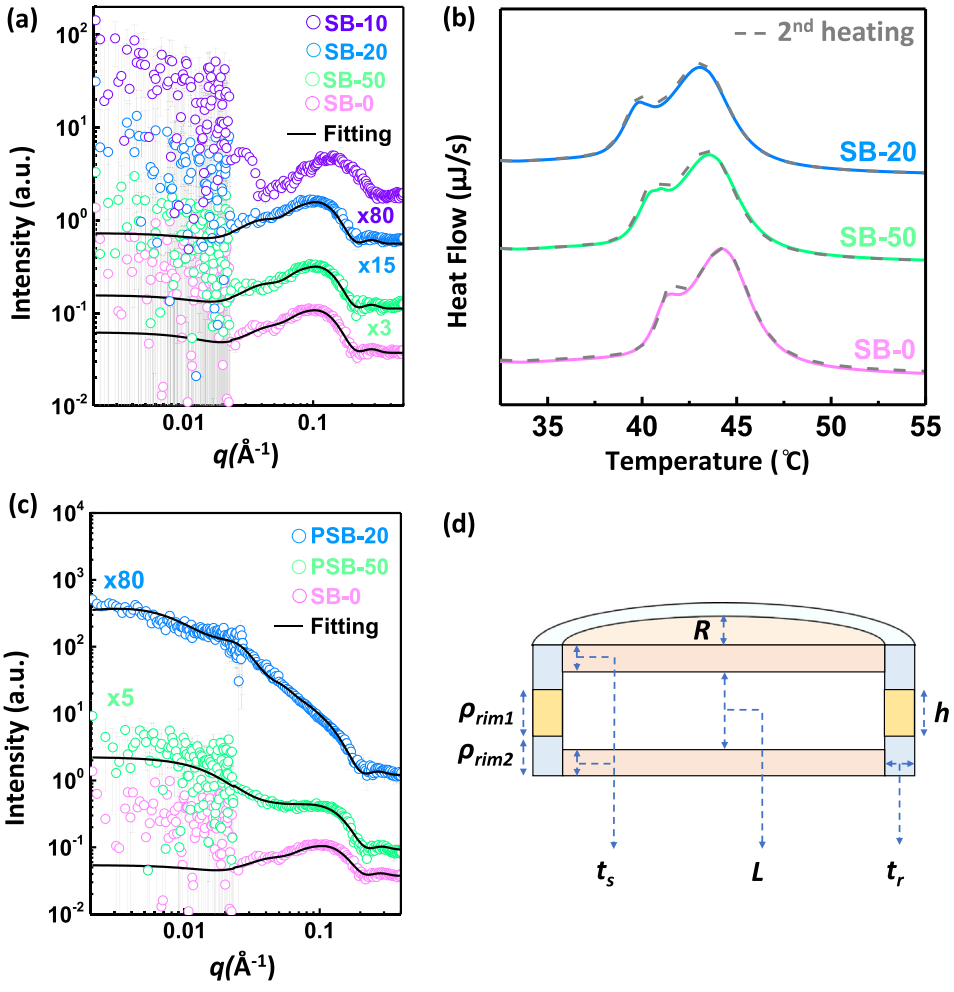

Fig. 3. (a) The SANS patterns of **SB-0**, **SB-50**, **SB-20**, and **SB-10**. The rescaling factors (shown at end of the curve) are applied for better clarity. (b) The DSC thermograms of before polymerization. (c) The SANS patterns of **SB-0**, **PSB-50**, and **PSB-20**. The rescaling factors (shown at end of the curve) are applied for better clarity. (d) The cross section of Sandwiched-Rim CSD (SR-CSD) model. R, t_s, t_r, L and h represent the core radius, shell thickness, rim thickness, hydrophobic length, and the height of the rim1, respectively. The ρ_{rim1} and ρ_{rim2} are NSLDs of rim 1 and 2, respectively.

All the CM samples were prepared at a C_{lp} of 20 wt% because of low scattering intensity. Note that perfect CM condition is not achievable due to the internal contrast of lipid bilayer as $\rho_{hydrophilic}$ and $\rho_{hydrophobic}$ cannot be simultaneously matched by $\rho_{solvent}$ [52]. Fig. 3(a) shows the SANS data of **SB-0**, **SB-50**, **SB-20**, and **SB-10** and their best fits using a core–shell discoidal (CSD) model (Fig. S1) to minimize the number of fitting parameters. The best fit of **SB-10** is not included in Fig. 3(a) because the system was converted into lamellae at C_{lp} = 10 wt% judged by the SAXS data (Fig. S5). As a result, our analysis mainly focuses on the **SB-50** and **SB-20**. The large error bars in low-q regime [Fig. 1(a)] originates from the low contrast between lipids and solvent at the CM condition.

The SANS data of **SB-0, SB-50** and **SB-20** are practically identical with no statistically significant difference in the best fitting parameters (Table 2) which are also in good agreement with the SAXS best-fitting outcomes (Table 1). Besides, ρ_{rim} is practically invari-

Table 2
The fitting results of **SB-0**, **SB-50**, and **SB-20** through the CSD model.

Sample	**SB-0**	**SB-50**	**SB-20**
R (Å)	85 ± 4	90 ± 4	90 ± 4
L (Å)	29 ± 1	29 ± 1	29 ± 1
t_r (Å)	18 ± 2	20 ± 2	20 ± 2
ρ_{core} (10^{-6} Å^{-2})	−0.37 ± 0.02	−0.34 ± 0.02	−0.34 ± 0.02
ρ_{rim} (10^{-6} Å^{-2})	0.1 ± 0.02	0.1 ± 0.02	0.1 ± 0.02
Reduced χ^2	0.8	0.9	1.6

ant after encapsulation of styrene-d_8 as larger hydrophobic foreign species tend to aggregate at the bicellar rim [37–39]. The similarity of scattering patterns of **SB-0**, **SB-50**, and **SB-20** suggests that the styrene is distributed in the bicelles homogeneously. The DSC thermograms of **SB-0**, **SB-con50**, and **SB-20** with a C_{lp} of 1 wt% [Fig. 3 (b)] yield two peaks, corresponding to the melting transition temperature of DPPC (T_m, the first peak) and bicelle-to-vesicle structural transformation temperature (T_{trans}, the second peak), respectively, as described in a recent report [53]. Both T_m and T_{trans} after best fit by Gaussian distributions (Fig. S6) decrease with increased styrene composition (Table 3), presumably caused by increased composition of styrene in DPPC, resulting in the bicellar discs prone to vesiculation [54]. Note that the DSC scans are reversible for all samples, indicating that not only the structure but also the distribution of styrene locations (i.e., at bilayer or rim) are *T*-, instead of path-, dependent.

Polymerization drastically changes the internal contrast of the disks judged by the SANS patterns of **PSB-50** and **PSB-20** [Fig. 3 (c)] in comparison with those of **SB-50** and **SB-20**. Although the CSD model was able to describe the SANS pattern well (Fig. S7), *unreasonable* best-fitting ρ_{rim} values were obtained (Table S1), resulting in the estimated styrene compositions about *an order of magnitude higher* than the corresponding as-prepared styrene amounts in **SB-50** and **SB-20**.

The *unrealistic* best-fitting values of ρ_{rim} originates from the assumption of a uniform rim in CSD model, which imposes the constraint that **PS** is homogeneously distributed in the rim, and thus the contrast is "falsely" increased leading to overestimating the composition of **PS** in the system. In order to correct this issue, a new Sandwiched-Rim CSD (SR-CSD) scattering model is developed with the flexibility of a composite rim made of a central **PS**-rich, rim1, vertically sandwiched by two symmetric lipid-rich, rim2 of the same width as depicted as shown in Fig. 3(d). The height and the NSLD of rim1 are assigned as h and ρ_{rim1}, respectively. During the fitting process, we minimize the number of fitting parameters by keeping the hydrophilic shell thickness (t_s), hydrophobic length (L), and NSLD of hydrophilic shell (ρ_{shell}) the same as the best fitting values obtained from **SB-0**, i.e., 13 Å, 27 Å, and 1.1 10^{-6} Å^{-2}, respectively. The NSLD of rim 2, ρ_{rim2} is also set the same as ρ_{rim} (=1.0×10^{-7} Å^{-2} based on **SB-0**). Note that a H-PMSA structure factor is required to describe the peak at $q \sim 0.023$ Å^{-1} in the case of **PSB-20** because of the deviation of contrast-matched condition at such high **PS** composition. Table 4 shows the best fitting values of ρ_{rim1} obtained from **PSB-50** and **PSB-20** are 4.0×10^{-7} Å^{-2} and 8.0×χ10^{-7} Å^{-2}, respectively, with

Table 4
The best fitted results of **SB-0**, **PSB-50**, and **PSB-20** by using SR-CSD model.

Sample	**SB-0**	**PSB-50**	**PSB-20**
Volume ratio of styrene-to-lipid (as-prepared value)	–	0.0032	0.0081
R (Å)	80 ± 5	80 ± 10	168 ± 5
t_r (Å)	19 ± 1	23 ± 3	55 ± 9
ρ_{core} (10^{-6} Å^{-2})	−0.45 ± 0.01	−0.2 ± 0.1	−0.3 ± 0.1
ρ_{rim1} (10^{-6} Å^{-2})	0.1 ± 0.02	0.4 ± 0.03	0.8 ± 0.02
h (Å)	–	8.5	8.5
Volume ratio of styrene-to-lipid (Based on fitting results)	–	0.003	0.0078
Reduced χ^2	1.2	2.0	2.9

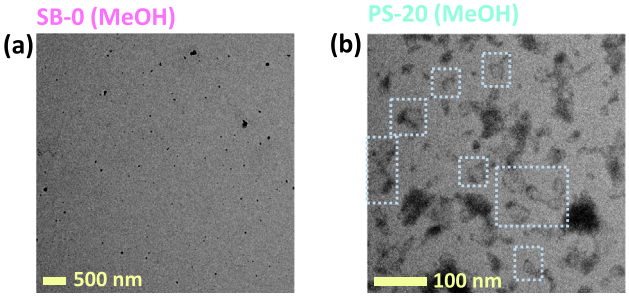

Fig. 4. The TEM micrographs of (a) **SB-0**, (b) **PS** nano-rings (**PSB-20**) after removal of phospholipids via MeOH. Noted that the samples are not negatively stained.

h = 8.5 Å, yielding the volume fractions of **PS** to be 0.0029 and 0.0078, respectively, similar to the added styrene in **SB-50** and **SB-20**. TEM images in Fig. 4 illustrate the **SB-0** and **PSB-20** after the removal of phospholipids with methanol (MeOH) washing as described in Materials and Methods. It clearly shows the structure of nano-rings as marked by the boxes of Fig. 4 (b) and the diameter of nano-rings is ∼ 300 (±80) Å agreeing with our interpretation of SAXS and SANS results. Noted that several black dots in Fig. 4(b) may result from the nano-ring aggregates due to the drying process or polymer complexed with lipid residues in the solution. More TEM images of **PS** nano-rings are presented in Fig. S8. One would expect the polymer nano-rings are not cyclic single chain but cross-linked **PS** due to the addition of DVB.

3.3. Thermal and wide-angle X-ray scattering measurement – the effect of nano-rings on lipids

The DSC data of **PSB-20** and **PSB-50** compared against that of **SB-0** further support the formation of **PS** nano-rings. Higher T_m values of **PSB-50** and **PSB-20** (i.e., ∼ 42 °C) than that of DPPC (41.3 °C) are obtained in contrast to the depression of T_m in **SB-50** and **SB-20** sample [Fig. 5(a), (b) and Table 3]. Moreover, the fact that $\Delta H_{m,DPPC}$ (the area underneath the T_m peak as shown in Fig. S9) of **PSB** series increases with increased styrene-to-lipid ratio, indicates that the gel-phase DPPC with higher **PS** composition requires more energy to melt. We have also performed DSC on the DPPC/DPPG/styrene vesicles (in the absence of short-chain DHPC) at

Table 3
The T_m of DPPC and T_{trans} of structural transformation* before and after polymerization.

Sample	Before polymerization		Sample	After polymerization	
	T_m (°C)	T_{trans} (°C)		T_m (°C)	T_{trans} (°C)
SB-0	41.3 ± 0.1	44.2 ± 0.2	**SB-0**	–	–
SB-50	40.6 ± 0.2	43.4 ± 0.2	**PSB-50**	42.0 ± 0.2	44.0 ± 0.1
SB-20	39.6 ± 0.2	42.9 ± 0.2	**PSB-20**	41.7 ± 0.2	44.0 ± 0.2

*The values are presented as average and standard deviation from two separate samples. The data were fitted from the second heating scan for each measurement.

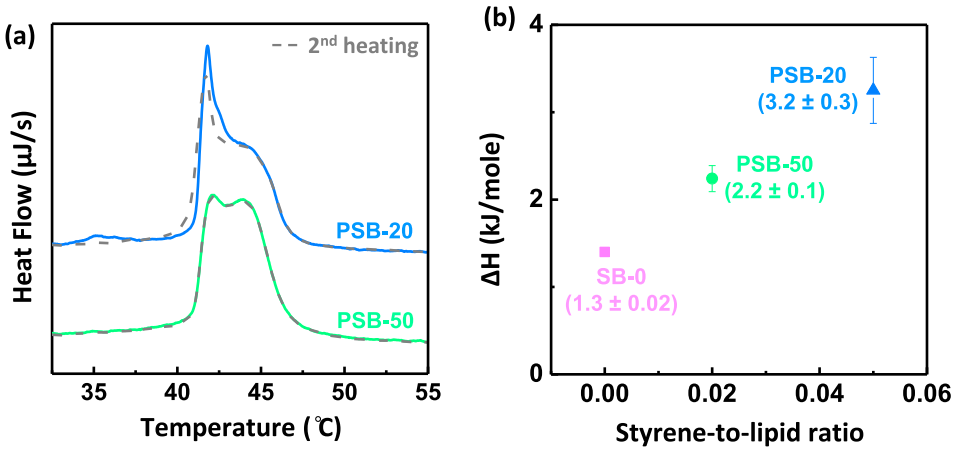

Fig. 5. (a) The DSC thermograms of **PSB-50** and **PSB-20**. (b) The enthalpy of **SB-0**, **PSB-50**, and **PSB-20**. The values are presented as average and standard deviation from two separate samples. The data were analyzed from the second heating scan for each measurement.

samples of styrene-to-DPPC ratios of 1:50 and 1:5 after polymerization (Fig. S10 and Table S2). The fact that the DPPC melting peak becomes broadened and the $\Delta H_{m,DPPC}$ decreases significantly with increased **PS** composition, suggestings reduction of cooperativity in DPPC gel phase as reported in literature [55]. Hence, the unique enhancement of both T_m and $\Delta H_{m,DPPC}$ in **PSB-20** and **PSB-50** can be rationalized by the increased lateral pressure imposed by cross-linked **PS** at the DHPC-rich rim. The narrower FWHM of the diffraction peak from the chain-chain correlation of DPPC for **PSB-20** and **PSB-50** samples in a wide-angle X-ray scattering experiment (Fig. S11 and Table S3) provides further evidence of larger domain of orderly-packed DPPC in presence of **PS** than pristine bicelles. The higher T_m, the greater $\Delta H_{m,DPPC}$ and the sharper WAXS peak of the chain-chain correlation from **PSB** samples compared to those from the corresponding **SB** samples confirm that **PS**, unlike styrene, segregates from the DPPC, indirectly suggesting the formation of a nano-ring that "belts" the bicelle.

3.4. The mechanism for the formation of polymer nano-rings

The aforementioned results not only demonstrate a protocol for the synthesis of well-defined PS nano-rings but also suggest several intriguing discoveries during the process. Upon self-assembly the monomers presumably mix with lipids forming the discoidal bicelles. Polymerization does not perturb the discoidal structure but draw monomers to the rim area, forming **PS** nano-rings.

The fundamental Flory-Huggins solution theory proves that high degree of polymerization reduces the entropy of polymer chain, increasing immiscibility between polymer and solvent. By the same reason, enhanced immiscibility between DPPC and **PS** is expected in comparison to that between DPPC and styrene monomers. Furthermore, the depletion of **PS** from the DPPC promotes crystallization of the DPPC gel phase, which further reduces the energy of the system. As a result, **PS** in the planar region migrates to more fluid DHPC-rich rim, which has been proven to be able to accommodate larger hydrophobic species such as supramolecules [38], Au nanoclusters [36,37], and quantum dots [39] due to the adjustable molecular curvature. The entrapped styrene in planar bilayer continues to diffuse to rim, feeding monomers to the active **PS** (with radicals), and eventually forming **PS** nano-rings. Our future study will extend to the controllable ring size through thermal annealing around T_m [33,56], leading to a robust well-controlled platform to synthesize polymer nano-rings. In spite of several examples of toroidal shape through the self-assembled with multi-step reactions in literature [27,57–64], a facile synthesis of polymer nano-rings is first-time reported here. It is noteworthy that the synthetic platform of nano-rings can be generalized for other hydrophobic polymers. We have used the same platform for three other monomers, i.e., vinyl acetate, dodecyl methacrylate, and 4 methyl styrene. All TEM micrographs (Fig. S12) indicate uniform discoidal structures after polymerization. Furthermore, the DSC thermograms consistently show enhanced T_m of DPPC (> 41 °C) as observed in the **PSB** (Fig. S13 and Table S4), demonstrating that this protocol can be a generalized synthetic platform to produce polymer nano-rings.

4. Conclusion

We have demonstrated a facile synthesis of well-defined polymer nano-rings, which are not accessible with conventional emulsion polymerization. [18] The bicelle, a robust self-assembly, serves as an excellent generalized template for controllable polymerization of nanoscale colloids [30]. The formation of nano-rings is attributed to the fact that the rim of bicellar discs is more "inclusive" to the foreign hydrophobic species with nanoscale than the planar region is [37–39]. The interpretation of CM SANS data and TEM images coherently confirm the formation of polymer nano-rings. The DSC thermograms further suggest demixing of polymers from long-chain lipids due to reduced entropy. The research outcome provides the insight into combinational effects of hydrophobic interactions, mismatched miscibility of polymers between the ordered and disordered phases, and crystallinity of the long lipid acyl chains on final morphology. Although toroidal-shape polymers could be synthesized from self-assembly of block copolymers or chiral azobenzene dimers with multi-step reactions [27,57–64], the facile synthesis of polymer nano-rings is the first-time presented here. The advanced methodology potentially changes the paradigm of polymerization to construct well-defined and well-controlled cnanoscale morphologies. The understanding of the formation mechanism is fundamentally important for general colloid, polymer and surfactant systems. Because a nano-ring has a high interfacial area, the structure will be an excellent building block for future applications in protein separation, catalyst design, electronic devices or nanomedicines after functionalization of the polymers. We aim to widen the controllable size range of the rings (e.g., > 100 nm) through thermal annealing [56], functionalize the side-group of polymers, synthesize Janus rings or conductive rings, which are not accessible in current colloidal synthesis.

Data availability

No data was used for the research described in the article.

Declaration of Competing Interest

The authors declare that they have no known competing financial interests or personal relationships that could have appeared to influence the work reported in this paper.

Acknowledgement

C.-H. Liu and M.-P. Nieh would like to acknowledge NSF (CBET 1930906) for the partial support for the project. The authors thank to the beamtime of 16ID-LiX at the NSLS-II (Brookhaven National Lab) through a beamtime proposal (BAG-302208). The LiX beamline is part of the Center for BioMolecular Structure (CBMS), which is primarily supported by the National Institutes of Health, National Institute of General Medical Sciences (NIGMS) through a P30 Grant (P30GM133893), and by the DOE Office of Biological and Environmental Research (KP1605010). LiX also received additional support from NIH Grant S10 OD012331. As part of NSLS-II, a national user facility at Brookhaven National Laboratory, work performed at the CBMS is supported in part by the U.S. Department of Energy, Office of Science, Office of Basic Energy Sciences Program under contract number DE-SC0012704. Access to SANS was provided by the Center for High Resolution Neutron Scattering, a partnership between the National Institute of Standards and Technology and the National Science Foundation under Agreement No. DMR-2010792.

Disclaim

Access to vSANS was provided by the Center for High Resolution Neutron Scattering, a partnership between the National Institute of Standards and Technology and the National Science Foundation under Agreement No. DMR-2010792. Certain commercial equipment, instruments, or materials (or suppliers, or software...) are identified in this paper to foster understanding. Such identification does not imply recommendation or endorsement by the National Institute of Standards and Technology, nor does it imply that the materials or equipment identified are necessarily the best available for the purpose.

Appendix A. Supplementary material

Supplementary data to this article can be found online at https://doi.org/10.1016/j.jcis.2022.09.141.

References

[1] H. Warson, Emulsion polymerization, a mechanistic approach. R. G. Gilbert. Academic Press, London, 1995. pp. xviii + 362, price £55.00. ISBN 0-12-283060-1, Polymer International 41(3) (1996) 352-352.
[2] P.A. Lovell, F.J. Schork, Fundamentals of emulsion polymerization, Biomacromolecules 21 (11) (2020) 4396–4441.
[3] Emulsion Polymerization, Principles of Polymerization, 2004, pp. 350–371.
[4] E. Bourgeat-Lami, M. Lansalot, Organic/inorganic composite latexes: the marriage of emulsion polymerization and inorganic chemistry, in: A.M. van Herk, K. Landfester (Eds.), Hybrid Latex Particles: Preparation With (Mini) emulsion Polymerization, Springer, Berlin Heidelberg, Berlin, Heidelberg, 2010, pp. 53–123.
[5] G. Qi, C.W. Jones, F.J. Schork, Enzyme-initiated miniemulsion polymerization, Biomacromolecules 7 (11) (2006) 2927–2930.
[6] P. Galanopoulo, N. Gil, D. Gigmes, C. Lefay, Y. Guillaneuf, M. Lages, J. Nicolas, M. Lansalot, F. D'Agosto, One-step synthesis of degradable vinylic polymer-based latexes via aqueous radical emulsion polymerization, Angew. Chem. Int. Ed. 61 (15) (2022) e202117498.
[7] J. Jang, K. Lee, Facile fabrication of hollow polystyrene nanocapsules by microemulsion polymerization, Chem. Commun. (10) (2002) 1098–1099.
[8] C.A. McKelvey, E.W. Kaler, J.A. Zasadzinski, B. Coldren, H.T. Jung, Templating hollow polymeric spheres from catanionic equilibrium vesicles: synthesis and characterization, Langmuir 16 (22) (2000) 8285–8290.
[9] J. Cui, Y. Wang, A. Postma, J. Hao, L. Hosta-Rigau, F. Caruso, Monodisperse polymer capsules: tailoring size, shell thickness, and hydrophobic cargo loading via emulsion templating, Adv. Funct. Mater. 20 (10) (2010) 1625–1631.
[10] A.M. van Herk, Vesicle-templated polymerization, a review, Biomacromolecules 21 (11) (2020) 4379–4387.
[11] D.C. Danila, L.T. Banner, E.J. Karimova, L. Tsurkan, X. Wang, E. Pinkhassik, Directed assembly of sub-nanometer thin organic materials with programmed-size nanopores, Angew. Chem. Int. Ed. 47 (37) (2008) 7036–7039.
[12] M.S. Silverstein, PolyHIPEs: recent advances in emulsion-templated porous polymers, Prog. Polym. Sci. 39 (1) (2014) 199–234.
[13] F. Duan, Y. Zhu, H. Yu, A. Wang, Porous materials fabricated from Pickering foams stabilized by natural plant of Angelica sinensis for removal of Cd (II) and Cu (II), Colloids Surf., A 648 (2022) 128695.
[14] M. Antonietti, K. Landfester, Polyreactions in miniemulsions, Prog. Polym. Sci. 27 (4) (2002) 689–757.
[15] A. Kabalnov, Ostwald ripening and related phenomena, J. Dispersion Sci. Technol. 22 (1) (2001) 1–12.
[16] M. Hu, T.P. Russell, Polymers with advanced architectures as emulsifiers for multi-functional emulsions, Mater. Chem. Front. 5 (3) (2021) 1205–1220.
[17] J. Tang, P.J. Quinlan, K.C. Tam, Stimuli-responsive Pickering emulsions: recent advances and potential applications, Soft Matter 11 (18) (2015) 3512–3529.
[18] K. Landfester, F.J. Schork, V.A. Kusuma, Particle size distribution in mini-emulsion polymerization, C. R. Chim. 6 (11) (2003) 1337–1342.
[19] F.M. Pavel, Microemulsion polymerization, J. Dispersion Sci. Technol. 25 (1) (2004) 1–16.
[20] C.J. Ferguson, R.J. Hughes, B.T.T. Pham, B.S. Hawkett, R.G. Gilbert, A.K. Serelis, C. H. Such, Effective ab initio emulsion polymerization under RAFT control, Macromolecules 35 (25) (2002) 9243–9245.
[21] N.J. Warren, S.P. Armes, Polymerization-induced self-assembly of block copolymer nano-objects via RAFT aqueous dispersion polymerization, J. Am. Chem. Soc. 136 (29) (2014) 10174–10185.
[22] E.E. Brotherton, F.L. Hatton, A.A. Cockram, M.J. Derry, A. Czajka, E.J. Cornel, P.D. Topham, O.O. Mykhaylyk, S.P. Armes, In situ small-angle X-ray scattering studies during reversible addition-fragmentation chain transfer aqueous emulsion polymerization, J. Am. Chem. Soc. 141 (34) (2019) 13664–13675.
[23] S.Y. Khor, N.P. Truong, J.F. Quinn, M.R. Whittaker, T.P. Davis, Polymerization-induced self-assembly: the effect of end group and initiator concentration on morphology of nanoparticles prepared via RAFT aqueous emulsion polymerization, ACS Macro Lett. 6 (9) (2017) 1013–1019.
[24] W.-J. Zhang, C.-Y. Hong, C.-Y. Pan, Formation of hexagonally packed hollow hoops and morphology transition in RAFT ethanol dispersion polymerization, Macromol. Rapid Commun. 36 (15) (2015) 1428–1436.
[25] F. Lv, Z. An, P. Wu, Scalable preparation of alternating block copolymer particles with inverse bicontinuous mesophases, Nat. Commun. 10 (1) (2019) 1397.
[26] W.-J. Zhang, C.-Y. Hong, C.-Y. Pan, Efficient fabrication of photosensitive polymeric nano-objects via an ingenious formulation of RAFT dispersion polymerization and their application for drug delivery, Biomacromolecules 18 (4) (2017) 1210–1217.
[27] H. Cui, Z. Chen, K.L. Wooley, D.J. Pochan, Origins of toroidal micelle formation through charged triblock copolymer self-assembly, Soft Matter 5 (6) (2009) 1269–1278.
[28] J. Wan, B. Fan, S.H. Thang, RAFT-mediated polymerization-induced self-assembly (RAFT-PISA): current status and future directions, Chem. Sci. 13 (15) (2022) 4192–4224.
[29] S.R. Mane, Trending methods employed for polymerization induced self-assembly, New J. Chem. 44 (17) (2020) 6690–6698.
[30] H.-P. Hentze, E.W. Kaler, Polymerization of and within self-organized media, Curr. Opin. Colloid Interface Sci. 8 (2) (2003) 164–178.
[31] Y. Liu, Y. Xia, A.T. Rad, W. Aresh, M.-P. Nieh, Stable discoidal bicelles: a platform of lipid nanocarriers for cellular delivery, in: G.G.M. D'Souza (Ed.), Liposomes: Methods and Protocols, Springer, New York, New York, NY, 2017, pp. 273–282.
[32] Y. Liu, M. Li, Y. Yang, Y. Xia, M.-P. Nieh, The effects of temperature, salinity, concentration and PEGylated lipid on the spontaneous nanostructures of bicellar mixtures, Biochim. Biophys. Acta (BBA) - Biomembranes 1838 (7) (2014) 1871–1880.
[33] M.-P. Nieh, P. Dolinar, N. Kučerka, S.R. Kline, L.M. Debeer-Schmitt, K.C. Littrell, J. Katsaras, Formation of kinetically trapped nanoscopic unilamellar vesicles from metastable nanodiscs, Langmuir 27 (23) (2011) 14308–14316.
[34] S. Tekobo, E. Pinkhassik, Directed covalent assembly of rigid organic nanodisks using self-assembled temporary scaffolds, Chem. Commun. (9) (2009) 1112–1114.
[35] S. Tekobo, A.G. Richter, S.A. Dergunov, S.V. Pingali, V.S. Urban, B. Yan, E. Pinkhassik, Synthesis, characterization, and controlled aggregation of biotemplated polystyrene nanodisks, J. Nanopart. Res. 13 (12) (2011) 6427–6437.
[36] H. Sharma, E.E. Dormidontova, Lipid nanodisc-templated self-assembly of gold nanoparticles into strings and rings, ACS Nano 11 (4) (2017) 3651–3661.
[37] A. Tahmasbi Rad, Y. Bao, H.-S. Jang, Y. Xia, H. Sharma, E.E. Dormidontova, J. Zhao, J. Arora, V.T. John, B.Z. Tang, T. Dainese, A. Hariri, J.V. Jokerst, F. Maran, M.-P. Nieh, Aggregation-enhanced photoluminescence and photoacoustics of

atomically precise gold nanoclusters in lipid nanodiscs (NANO2), Adv. Funct. Mater. 31 (10) (2021) 2009750.
[38] C.-H. Liu, H. Wang, L. Yang, Y. Liu, X. Li, M.-P. Nieh, Nanocomplex made up of antimicrobial metallo-supramolecules and model biomembranes – characterization and enhanced fluorescence, Nanoscale 13 (35) (2021) 14973–14979.
[39] J.M. Fang, S. Basu, M. Li, K.-C. Shih, J. Wang, M. Cotlet, X. Wang, J. Zhao, T.J. Mountziaris, J.J. LoTurco, M.-P. Nieh, Restriction-in-motion of surface ligands enhances photoluminescence of quantum dots—experiment and theory, Adv. Mater. Interfaces 9 (6) (2022) 2102079.
[40] M.-P. Nieh, V.A. Raghunathan, G. Pabst, T. Harroun, K. Nagashima, H. Morales, J. Katsaras, P. Macdonald, Temperature driven annealing of perforations in bicellar model membranes, Langmuir 27 (8) (2011) 4838–4847.
[41] M.P. Nieh, V.A. Raghunathan, H. Wang, J. Katsaras, Highly aligned lamellar lipid domains induced by macroscopic confinement, Langmuir 19 (17) (2003) 6936–6941.
[42] M.-P. Nieh, C.J. Glinka, S. Krueger, R.S. Prosser, J. Katsaras, SANS study on the effect of lanthanide ions and charged lipids on the morphology of phospholipid mixtures, Biophys. J. 82 (5) (2002) 2487–2498.
[43] V.A. Bhanu, K. Kishore, Role of oxygen in polymerization reactions, Chem. Rev. 91 (2) (1991) 99–117.
[44] Y. Okazaki, H. Jintoku, M. Takafuji, R. Oda, H. Ihara, Creation of a polymer backbone in lipid bilayer membrane-based nanotubes for morphological and microenvironmental stabilization, RSC Adv. 4 (63) (2014) 33194–33197.
[45] L. Yang, Using an in-vacuum CCD detector for simultaneous small- and wide-angle scattering at beamline X9, J. Synchrotron Radiation 20 (2) (2013) 211–218.
[46] J.S. Higgins, H.C. Benoit, Polymers and Neutron Scattering, Oxford Science Publications, United Kingdom, 1994.
[47] Available from: <https://www.rigaku.com/support/software/pdxl>.
[48] C. Cheu, L. Yang, M.-P. Nieh, Refining internal bilayer structure of bicelles resolved by extended-q small angle X-ray scattering, Chem. Phys. Lipids (2020) 104945.
[49] J.B. Hayter, J. Penfold, An analytic structure factor for macroion solutions, Mol. Phys. 42 (1) (1981) 109–118.
[50] J.-P. Hansen, J.B. Hayter, A rescaled MSA structure factor for dilute charged colloidal dispersions, Mol. Phys. 46 (3) (1982) 651–656.
[51] C.Z. Tingting Li, Ming Jian, UV absorption spectra of polystyrene, Polym. Bull. (25) (1991) 211–216.
[52] M.-P. Nieh, C.J. Glinka, S. Krueger, R.S. Prosser, J. Katsaras, SANS study of the structural phases of magnetically alignable lanthanide-doped phospholipid mixtures, Langmuir 17 (9) (2001) 2629–2638.
[53] I. Alahmadi, D. Hoy, A. Tahmasbi Rad, S. Patil, A. Alahmadi, J. Kinnun, H.L. Scott, J. Katsaras, M.-P. Nieh, Changes experienced by low-concentration lipid Bicelles as a function of temperature, Langmuir 38 (14) (2022) 4332–4340.
[54] M.-P. Nieh, N. Kučerka, J. Katsaras, Chapter 1 - Spontaneously Formed Unilamellar Vesicles, Methods in Enzymology, Academic Press, 2009, pp. 3–20.
[55] M.I. Morandi, M. Kluzek, J. Wolff, A. Schroder, F. Thalmann, C.M. Marques, Accumulation of styrene oligomers alters lipid membrane phase order and miscibility, Proc. Natl. Acad. Sci. 118 (4) (2021) e2016037118.
[56] S. Mahabir, D. Small, M. Li, W. Wan, N. Kučerka, K. Littrell, J. Katsaras, M.-P. Nieh, Growth kinetics of lipid-based nanodiscs to unilamellar vesicles—a time-resolved small angle neutron scattering (SANS) study, Biochim. Biophys. Acta (BBA) - Biomembranes 1828 (3) (2013) 1025–1035.
[57] A. Steinhaus, R. Chakroun, M. Müllner, T.-L. Nghiem, M. Hildebrandt, A.H. Gröschel, Confinement assembly of ABC triblock terpolymers for the high-yield synthesis of Janus nanorings, ACS Nano 13 (6) (2019) 6269–6278.
[58] J.-K. Kim, E. Lee, Z. Huang, M. Lee, Nanorings from the self-assembly of amphiphilic molecular dumbbells, J. Am. Chem. Soc. 128 (43) (2006) 14022–14023.
[59] S. Yagai, M. Yamauchi, A. Kobayashi, T. Karatsu, A. Kitamura, T. Ohba, Y. Kikkawa, Control over hierarchy levels in the self-assembly of stackable nanotoroids, J. Am. Chem. Soc. 134 (44) (2012) 18205–18208.
[60] P. Xu, L. Gao, C. Cai, J. Lin, L. Wang, X. Tian, Helical toroids self-assembled from a binary system of polypeptide homopolymer and its block copolymer, Angew. Chem. Int. Ed. 59 (34) (2020) 14281–14285.
[61] J. Kang, J. Zhu, J. Lin, C. Han, K. Liu, X. Wang, Ring size-dependent solution behavior of macrocycles: dipole-dipole attraction counteracted by excluded volume repulsion, Macromolecules 54 (16) (2021) 7441–7447.
[62] H. Huang, B. Chung, J. Jung, H.-W. Park, T. Chang, Toroidal micelles of uniform size from diblock copolymers, Angew. Chem. Int. Ed. 48 (25) (2009) 4594–4597.
[63] P. Xu, L. Gao, C. Cai, J. Lin, L. Wang, X. Tian, Polymeric toroidal self-assemblies: diverse formation mechanisms and functions, Adv. Funct. Mater. 32 (1) (2022) 2106036.
[64] L.J. Endter, H.J. Risselada, Where are those lipid nano rings?, J Colloid Interface Sci. 587 (2021) 789–796.